Electrochemically-Driven Water Oxidation by a Highly Active Ruthenium-Based Catalyst

Andrey Shatskiy,[a] Andrey A. Bardin,[a, b] Michael Oschmann,[a] Roc Matheu,[c] Jordi Benet-Buchholz,[c] Lars Eriksson,[d] Markus D. Kärkäs,[e] Eric V. Johnston,[a, f] Carolina Gimbert-Suriñach,[c] Antoni Llobet,*[c, g] Björn Åkermark*[a]

Abstract: Herein is described a highly active ruthenium-based water oxidation catalyst [Ru^{X}(mcbp)(OH_n)($py)_2$] (**5**, $mcbp^{2-}$ = 2,6-bis(1-methyl-4-(carboxylate)benzimidazol-2-yl)pyridine; n = 2, 1, and 0 for X = II, III, and IV, respectively), which can be generated in a mixture of Ru^{III}/Ru^{IV} states from either [Ru^{II}(mcbp)($py)_2$] (**4^{II}**) or [Ru^{III}(Hmcbp)($py)_2]^{2+}$ (**4^{III}**). Complexes **4^{II}** and **4^{III}** were isolated and characterized by single crystal X-ray analysis, NMR, UV-vis, FT-IR, ESI-HRMS, EPR, and elemental analysis, and their redox properties were studied in detail by electrochemical and spectroscopic methods. Unlike for the parent catalyst [Ru(tda)($py)_2$] (**1**, tda^{2-} = [2,2′:6′,2″-terpyridine]-6,6″-dicarboxylate), for which full transformation to the catalytically active species [Ru^{IV}(tda)(O)($py)_2$] (**2**) could not be carried out — stoichiometric generation of the catalytically active Ru-aqua complex **5** from **4^{II}** was achieved under mild conditions (pH 7.0) and short reaction times. The redox properties of the catalyst were studied and its activity for electrocatalytic water oxidation was evaluated, reaching TOF_{max} ≈ 40 000 s^{-1} at pH 9.0 (from the foot-of-the-wave analysis, FOWA), which is comparable to the activity of the state-of-the-art catalyst **2**.

[a] *Dr. A. Shatskiy, Dr. A. A. Bardin, M. Oschmann, Dr. E. V. Johnston, Prof. B. Åkermark*
Department of Organic Chemistry, Arrhenius Laboratory, Stockholm University
Svante Arrhenius väg 16C, 10691 Stockholm (Sweden)
E-mail: bjorn.akermark@su.se
[b] *Dr. A. A. Bardin*
Current address:
Institute of Problems of Chemical Physics, Russian Academy of Sciences
Prospekt Akademika Semenova 1g, 142432 Chernogolovka, Moscow Region (Russia)
[c] *Dr. R. Matheu, Dr. J. Benet-Buchholz, Dr. C. Gimbert-Suriñach, Prof. A. Llobet*
Institute of Chemical Research of Catalonia (ICIQ), Barcelona Institute of Science and Technology (BIST)
Avinguda Països Catalans 16, 43007 Tarragona (Spain)
E-mail: allobet@iciq.cat
[d] *Assoc. Prof. L. Eriksson*
Department of Materials and Environmental Chemistry, Arrhenius Laboratory, Stockholm University
Svante Arrhenius väg 16C, 10691 Stockholm (Sweden)
[e] *Asst. Prof. M. D. Kärkäs*
Department of Chemistry, Organic Chemistry, KTH Royal Institute of Technology
Teknikringen 30, 10044 Stockholm (Sweden)
[f] *Dr. E. V. Johnston*
Current address:
Sigrid Therapeutics AB
Sankt Göransgatan 159, 11217 Stockholm (Sweden)
[g] *Prof. A. Llobet*
Departament de Química, Universitat Autònoma de Barcelona
Cerdanyola del Vallès, 08193 Barcelona (Spain)

Supporting Information and the ORCID identification numbers for the authors of this article can be found under http://dx.doi.org/

1. Introduction

Harvesting the energy of the Sun for the production of renewable fuels is identified as one of the prominent solutions for reducing the negative environmental effects caused by the use of fossil fuels.[1] For successful implementation of this process several challenges remain unsolved. One is the development of an efficient and durable water oxidation catalyst (WOC), which could promote the four-electron four-proton oxidation of water into molecular oxygen (Eq. 1).

$$2H_2O \rightarrow O_2 + 4H^+ + 4e^- \ (E^\circ = 1.23 \text{ V vs. NHE; pH 0}) \quad (1)$$

A number of heterogeneous and homogeneous (molecular) WOCs have been developed over the past two decades, with ruthenium-based molecular catalysts serving as the principal model for understanding the water oxidation mechanistic pathways.[2] As a result, a number of considerations for rational design of high performance molecular WOCs have been identified. These include: (1) the use of oxidatively stable organic ligands, with the nitrogen-containing aromatic heterocycles being the most common; (2) ability of the catalyst to undergo proton-coupled electron transfer (PCET), allowing generation of the high oxidation states of the catalytically active species at low potentials; (3) the use of redox non-innocent ligands, which can increase the stability of the catalyst while facilitating access to high formal oxidation states of the metal center; (4) the use of ligands, which can promote formation of seven-coordinated ruthenium-aqua species, thereby lowering the potentials of the relevant redox couples; (5) introduction of an internal base in the second coordination sphere of the metal center, which can assist the O–O bond formation via water nucleophilic attack (WNA) by simultaneous abstraction of a proton from water (intramolecular atom-proton transfer, *i*-APT); (6) for catalysts which form the O–O bond via radical coupling of two metal-oxo units (I2M mechanism) the ligand should promote the intermolecular reaction via hydrophobic or other interactions, or combine the two metal-oxo moieties within one molecule for efficient intramolecular reaction. Applying the above conside-

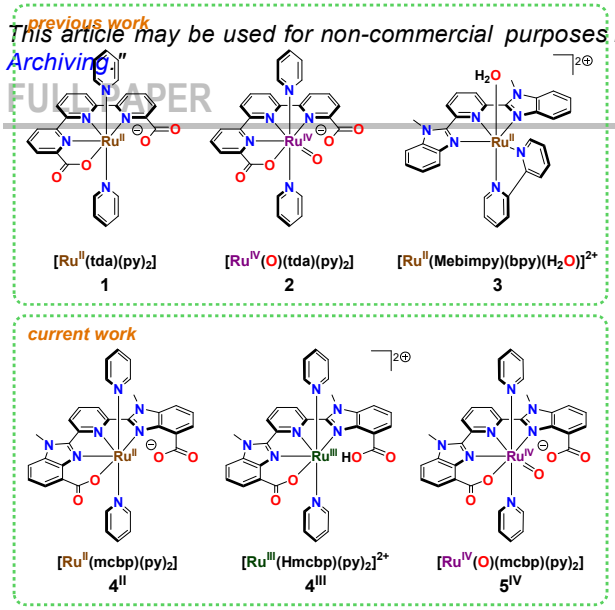

Figure 1. Structures of the previously synthesized ruthenium complexes (**1**, **2**, and **3**) and the complexes synthesized in the current work (**4^{II}**, **4^{III}** and **5^{IV}**).

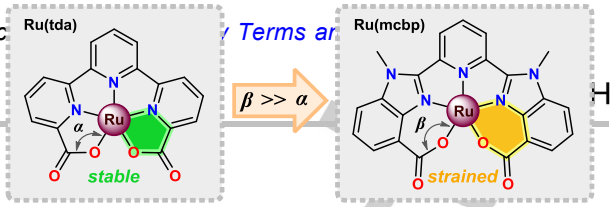

Figure 2. Schematic representation of the coordination mode of $[Ru(tda)(py)_2]^{n+}$ (*left*) and $[Ru(mcbp)(py)_2]^{n+}$ (*right*) complexes at Ru^{III} and Ru^{IV} states. The geometries of the complexes are adopted from the previously published crystal structures of complex **1** with direct extrapolation of the geometry for the structure of $[Ru(mcbp)(py)_2]^{n+}$. Axial pyridine ligands are omitted for clarity.

rations to the design of molecular WOCs, an increase in the turnover frequency (TOF) by seven orders of magnitude and the turnover number (TON) by three orders of magnitude has been achieved over the past decade. However, the long-term stability and operating potentials of the developed catalysts remains unsatisfactory and a commercially viable molecular WOC is yet to be designed.

Catalyst **1** ($[Ru(tda)(py)_2]$, tda^{2-} = [2,2′:6′,2″-terpyridine]-6,6″-dicarboxylate) has been recently developed by Llobet and co-workers, guided by most of the aforementioned design principles (Figure 1).[3] Catalyst **2**, the active form of catalyst **1**, demonstrated a record high activity for electrocatalytic water oxidation (TOF_{max} = 50 000 s^{-1} at pH 10, using foot-of-the-wave analysis, FOWA),[3a] as well as high longevity (TON = 1 000 000 under bulk electrolysis with a surface-immobilized catalyst).[3b] Moreover, the catalyst demonstrated high efficiency for light-driven water oxidation with the use of a $Ru(bpy)_3$-type photosensitizer in solution,[3c] as well as immobilized on hybrid semiconductor surfaces.[3d,f] The remarkable performance of the catalyst is attributed to the ability of the tda^{2-} ligand to facilitate formation of seven-coordinated Ru^{III}, Ru^{IV}, and Ru^{V} species at low overpotentials. Further, the dangling carboxylate group in complex **2** acts as an internal base, opening low-energy *i*-APT pathway during the rate-limiting O–O bond formation step. However, a significant drawback of the catalyst was the incomplete formation of the catalytically active Ru-aqua species **2** from the initial catalyst, rendering ⅔ of the used catalyst inactive during catalysis, which also obscured the mechanistic studies and decreased its performance when incorporated in hybrid anodes.[3a,b,d]

Catalyst **3** represents a well-studied ruthenium-based WOC developed by Meyer and co-workers (Figure 1).[4a,b] Although the catalyst had a moderate activity for electrocatalytic water oxidation, it served as a primary model for development of a number of strategies for the coupling of WOCs to a photosensitizer or the electrode surface[4c-h] and was subjected to detailed mechanistic studies.[4i-n] The related catalyst $[Ru^{II}(Mebimpy)(pic)_3]^{2+}$ (Mebimpy = 2,6-bis(1-methylbenzimidazol-2-yl)pyridine, pic = 4-picoline) has also been prepared by Sun and co-workers; however, it demonstrated no activity for electrocatalytic water oxidation at acidic or neutral pH.[5]

In the current work we sought to address the incomplete activation of complex **1** by preparing a ligand related to H_2tda, in which two of the coordinating pyridine moieties are substituted with 1-methylbenzimidazoles, similar to catalyst **3**. In the proposed catalyst **4** introduction of one more carbon between the coordinating nitrogen and carboxy-group was expected to cause significant structural changes for the complex at the Ru^{III} and Ru^{IV} oxidation states, where the original tda^{2-} ligand coordinates to the ruthenium center in a $\kappa\text{-}N^3O^2$ mode. Thus five-membered rings in catalyst **1** would expand to highly-distorted six-membered rings in catalyst **4**, assuming a $\kappa\text{-}N^3O^2$ coordination mode (Figure 2). This distortion was expected to weaken the Ru–O bonds in the complex, allowing easier access to the catalytically active aqua-species for catalyst **4** compared to catalyst **1**. Indeed, full conversion of the initial complex to the Ru-aqua species could be carried out for complex **4**, resulting in a highly active water oxidation catalyst **5**, reaching TOF_{max} values comparable to those of catalyst **1**. The structure of catalyst **5** was proposed based on analogy to catalyst **2**, and is fully consistent with the obtained experimental results.

Herein, we describe the preparation and redox properties of complex **4** in the Ru^{II} oxidation state (**4^{II}**) and its one-electron oxidized form **4^{III}** with an emphasis on formation of Ru-aqua species at the Ru^{III} and Ru^{IV} oxidation states of the complex. Furthermore, stoichiometric generation of complex **5** (herein also referred to as Ru-aqua species) during spectroelectrochemical measurements and bulk electrolysis is described, followed by analysis of its redox properties and catalytic activity for water oxidation.

2. Results

2.1 Synthesis and Characterization

The H_2mcbp (mcbp^{2-} = 2,6-bis(1-methyl-4-(carboxylate)-benzimidazol-2-yl)pyridine) ligand was synthesized via reductive cyclization between 2,6-pyridinedicarbox-aldehyde and methyl 3-(methylamino)-2-nitrobenzoate followed by hydrolysis of the formed ester. The Ru^{II} complex **4^{II}** ([Ru^{II}(mcbp)(py)$_2$]) was then obtained by a prolonged reaction between the H_2mcbp ligand, pyridine, and [Ru(DMSO)$_4$Cl$_2$] as ruthenium precursor in EtOH:water in the presence of NEt_3 as base (see the Supporting Information for details). X-ray quality crystals of **4^{II}** were isolated from the reaction mixture and the structure of the complex was confirmed by 1D and 2D NMR, SC-XRD, ESI-HRMS, elemental analysis, EPR, ATR-FTIR and UV-vis. Oxidation of Ru^{II} complex **4^{II}** by 1 equivalent of ceric ammonium nitrate (CAN) in the presence of $NaClO_4$ furnished the corresponding Ru^{III} complex **4^{III}** ([Ru^{III}(Hmcbp)(py)$_2$](ClO$_4$)$_2$). The complex was isolated as X-ray quality crystals by recrystallization from the solution in TFE (2,2,2-trifluoroethanol) and aqueous 0.1 M TfOH containing $NaClO_4$, and the structure of the complex was confirmed by ^{1}H NMR, SC-XRD, elemental analysis, EPR, ATR-FTIR and UV-vis. All attempts to synthesize the complex in the Ru^{IV} oxidation state were unsuccessful and resulted in isolation of Ru^{III} complexes, such as **4^{III}(OTf)$_2$** ([Ru^{III}(Hmcbp)(py)$_2$](OTf)$_2$), based on SC-XRD analysis. The Ru^{III} complex is presumably generated by slow oxidation of TFE or MeOH co-solvent by the initially formed Ru^{IV} complex.

A solution of catalyst **4^{II}** in DMSO-d_6 displayed a diamagnetic ^{1}H NMR spectrum, as expected for a d^6 Ru^{II} complex (Figure S11, top).[3a,4b,5] Initially, NMR signals from multiple species were observed, but a clear spectrum could be obtained upon addition of D_2SO_4 (Figure S11, bottom). The integrity of the complex composition under these conditions was confirmed by HPLC-ESI-MS. The ^{1}H NMR spectrum of **4^{II}** suggests a highly symmetric structure, indicative of a fast coordination/dissociation of the carboxylate groups to the metal center. The combination of ^{1}H NMR, ^{13}C NMR, ^{1}H-^{1}H COSY and HSQC experiments allowed for full assignment of the NMR spectra (Figure S13). The ^{1}H NMR spectrum of complex **4^{III}** displayed broadened and shifted peaks, characteristic of a paramagnetic d^5 Ru^{III} species (Figure S18).[3a,6] Reduction of this Ru^{III} complex to the Ru^{II} state with ascorbic acid resulted in a ^{1}H NMR spectrum identical to that of complex **4^{II}** (Figure S19).

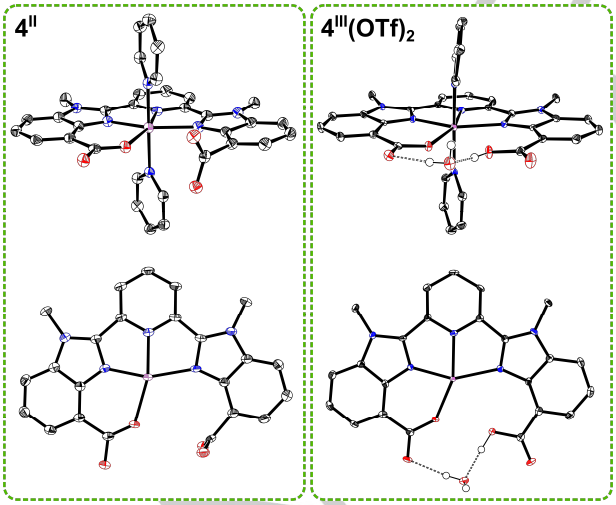

Figure 3. ORTEP plots (ellipsoids at 50% probability) of complexes **4^{II}** and **4^{III}(OTf)$_2$**. Hydrogen bonds are shown as black dashed lines and hydrogen atoms of the carboxy-group and water molecule are shown as black hollow circles. Other hydrogen atoms, solvent molecules and counter-ions are omitted for clarity. Axial pyridine ligands are omitted in the lower structures. Color codes: C — black, N — blue, O — red, Ru — magenta.

2.2 Single Crystal X-ray Analysis

X-ray structures of complexes **4^{II}** and **4^{III}(OTf)$_2$** are presented in Figure 3. In **4^{II}** the equatorial mcbp^{2-} ligand is coordinated to the metal center in a κ-N^{3}O fashion, while two pyridine ligands occupy the axial positions. For this complex a distorted octahedral geometry is observed with typical Ru–N and Ru–O bond lengths (see Table S4 for the comparison of relevant bond lengths and angles). For the isolated Ru^{III} complex **4^{III}** symmetry-related carboxylic groups were disordered into two positions (Figure S52, see the Supporting Information for details), while such a disorder was not observed in the crystal of **4^{III}(OTf)$_2$**. The structure of the latter complex was therefore used for further discussion.

The equatorial tda^{2-} ligand in the previously described [Ru^{III}(tda)(py)$_2$]$^+$ complex coordinates to ruthenium in a κ-N^{3}O^2 fashion. In contrast, the Hmcbp$^-$ ligand in **4^{III}(OTf)$_2$** adopts κ-N^{3}O coordination mode with one of the carboxy-groups being protonated and stabilized by a water molecule via hydrogen bonding, leading to a highly distorted octahedral geometry with a large O–Ru–N outer equatorial angle of 125°. Such a geometry is consistent with easier access to the catalytically-active Ru-aqua species for complex **4** relative to complex **1**, discussed in the following sections. It is, however, unclear if such a low symmetry structure is preserved in solution, particularly for fully deprotonated complexes in the Ru^{III} and Ru^{IV} oxidation states, where either κ-N^{3}O^2 coordination mode of the mcbp^{2-} ligand or fast coordination/dissociation of the two carboxy-groups to the metal center is to be expected.

2.3 Electrochemical and Spectroscopic Studies of Complexes 4^{II} and 4^{III} at pH 2–7

The electrochemical properties of the synthesized complexes were mainly studied in phosphate buffered solutions (0.1 ionic strength), using glassy carbon disk working electrode (d = 1 mm, S = 7.85×10^{-3} cm^2), platinum disk auxiliary electrode, and mercury-mercurous sulfate reference electrode (MSE, Hg/Hg_2SO_4, sat. K_2SO_4). All potentials were converted to vs. NHE by adding 0.650 V to the potentials vs. MSE. The redox properties of the complexes were studied by cyclic voltammetry

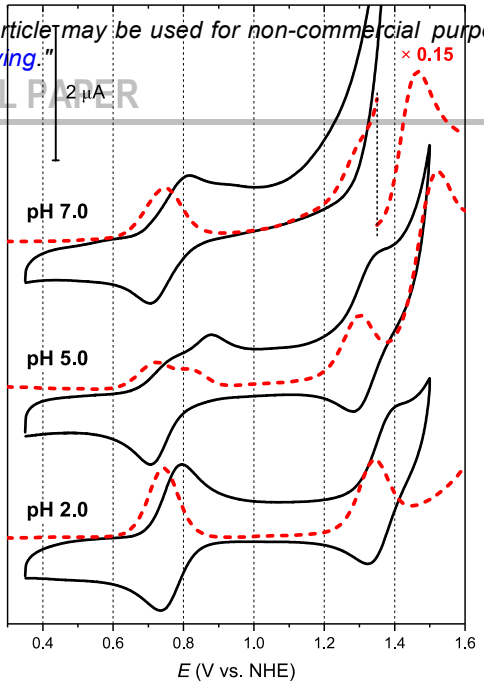

Figure 4. CV (black) and DPV (dashed red) of 0.1 mM solutions of complex $\mathbf{4}^{II}$ at pH 2.0, 5.0, and 7.0. Three CV cycles were recorded at 0.05 V s^{-1} scan rate between 0.3 V and 1.5 V and the last cycle is pre-sented for clarity.

(CV), differential pulse voltammetry (DPV), coulometry (controlled potential electrolysis, CPE), and spectro-electrochemistry (see the Supporting Information for details). Furthermore, the isolated and in situ generated complexes were analyzed under similar conditions by ^{1}H NMR, UV-vis spectroscopy, and EPR, recorded at 4 K with an X-band spectrometer. Due to limited solubility of the complexes in aqueous media the experiments were typically performed using 0.05–0.2 mM solutions.

2.3.1 Redox Properties of Ru^{II} Complex 4^{II}

At pH 2.0, the CV of complex $\mathbf{4}^{II}$ displayed two quasi-reversible one-electron waves at 0.767 V and 1.357 V, which are assigned to the $Ru^{III/II}$ and $Ru^{IV/III}$ couples, respectively (Figure 4). The one-electron nature of the couples is confirmed by the peak separation in the CV (ΔE_p, 0.059 V for $Ru^{III/II}$ and 0.068 V for $Ru^{IV/III}$), peak width at half-height in DPV ($W_{1/2}$, 0.096 V for $Ru^{III/II}$ and 0.094 V for $Ru^{IV/III}$),[7] and CPE for the $Ru^{III/II}$ couple (transfer of 1.0 electrons upon CPE at 1.05 V). Spectroelectrochemical measurements at pH 2.0 revealed the disappearance of the typical MLCT band for Ru^{II} complexes (λ_{max} = 495 nm for $\mathbf{4}^{II}$) upon the $Ru^{II}\rightarrow Ru^{III}$ transition (Figures S42 and S43a).[8] At higher potentials, a transition to a Ru^{IV} species was observed with two isosbestic points at 313 nm and 399 nm (Figure S43b) and a good charge balance with the $Ru^{II}\rightarrow Ru^{III}$ transition (Figure S42). During the reverse CV scan, the UV-vis spectra of both Ru^{III} and Ru^{II} species were replenished in their initial form, demonstrating reversibility of the involved transformations on the experiment timescale (Figures S43c and S43d).[9] Interestingly, the potential of the $Ru^{III/II}$ couple of $\mathbf{4}^{II}$ in an aprotic solvent (MeCN) was smaller than in aqueous solutions by ca. 0.3 V, but gradually shifted to the value observed in aqueous solutions upon addition of water (Figures S39 and S40), highlighting the importance of the hydrogen bonding interactions in the complex.

Upon increasing the pH, the potentials of the $Ru^{III/II}$ and $Ru^{IV/III}$ couples displayed a pH dependence of −0.019 and −0.030 V per pH unit over pH 3–4 and pH 2–3, respectively, while −0.059·*m* V per pH unit is expected for a one-electron processes involving transfer of *m* protons.[10] Such behavior can be rationalized assuming close pK_a values for complex **4** at the Ru^{II}, Ru^{III}, and Ru^{IV} oxidation states, involving protonation/deprotonation of one of the carboxylate groups. Indeed, simulation and fitting of the Pourbaix diagram to the experimental values according to Eq. S1 and S2 reveals that at low pH complex **4** at the Ru^{II}, Ru^{III}, and Ru^{IV} states is protonated with the pK_a = 4.0, 3.3 and 2.1, respectively (Figure S32, see the Supporting Information for details). The change in protonation state for the $Ru^{III/II}$ couple is then likely to be responsible for splitting of initially quasi-reversible $Ru^{III/II}$ wave into a pair of close-lying irreversible waves (ΔE_p = 0.110 V at pH 7.0, 0.05 V s^{-1} scan rate) and formation of an $E_rC_rE_rC_r$ square scheme upon increasing the pH (Figures 4 and S31).[11] Accordingly, at high scan rates the chemical reactions following/preceding the electron transfer can be outrun and a close-lying pair of two quasi-reversible $Ru^{III/II}$ couples is observed (Figure S33). This implies the presence of two isomers of the Ru^{II} complex at elevated pH. As the potentials for the Pourbaix diagram of $Ru^{III/II}$ transition were derived from E_{pc} of the electrochemically irreversible $Ru^{III/II}$ couple, the obtained pK_a value represents the pK_a^{II} of an isomer of complex **4**, dominant at the Ru^{III} state. The pK_a^{II} value of an isomer of **4** dominant at Ru^{II} oxidation state was then obtained by spectrophotometric pH titration and fitting of the experimental data to Eq. S3, resulting in a slightly different pK_a = 3.1 (Figure S27). At pH > 7 the electrochemical behavior of $Ru^{III/II}$ couple becomes more complex due to formation of the corresponding Ru-aqua species (*vide infra*). Therefore, the redox behavior of the complex at high pH was only studied for the electrochemically generated Ru-aqua species, as described in Section 2.4.2.

At pH > 3.5 a new wave for complex $\mathbf{4}^{II}$ appears in the DPV at high potentials (E > 1.4 V) while an electrocatalytic wave starts growing in the CV (Figure S31). Interestingly, at pH 7.0 the catalytic wave displayed an inverse loop and the catalytic current was growing upon repetitive cycling, which could indicate that the initially inactive form of complex **4** is transformed into an active catalyst at high potentials (Figure S35, *left*). Moreover, formation of new species with E_{pa} = 0.95 V could be observed upon repetitive cycling (Figure S35, *right*). This new species was assigned to the catalytically active Ru-aqua complex, generated from complex **4** when oxidized to the Ru^{IV} state (*vide infra*).

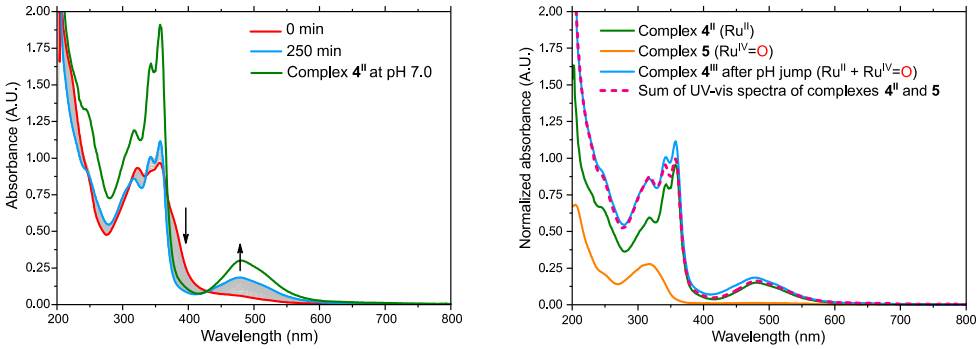

Figure 5. *Left*: Evolution of the UV-vis spectrum of 0.05 mM solution of complex $\mathbf{4^{III}}$ upon pH jump from pH 2.0 to 7.0 over 250 min (0 min — red line, 250 min — blue line) and a UV-vis spectrum of 0.05 mM solution of complex $\mathbf{4^{II}}$ at pH 7.0. *Right*: UV-vis spectra of complexes $\mathbf{4^{II}}$ (green line), $\mathbf{5^{IV}}$ (orange line, obtained from spectroelectrochemical measurements, see Section 2.4.1), their sum (dashed pink), and a UV-vis spectrum of complex $\mathbf{4^{III}}$ at 4 h after the pH jump (blue line). For the latter plot the absorbance of complex $\mathbf{4^{II}}$ was normalized for 0.025 mM concentration and absorbance of complex $\mathbf{5^{IV}}$ was normalized for 0.0125 mM concentration.

2.3.2 Redox Properties of Ru^{III} Complex 4^{III}

As expected, at pH 2.0 the electrochemical behavior of complex $\mathbf{4^{III}}$ was identical to that of complex $\mathbf{4^{II}}$ (Figure S36). The oxidation state of the complex was confirmed by CPE at 0.450 V, upon which transfer of 0.82 electrons was observed. The UV-vis spectrum of complex $\mathbf{4^{III}}$ at this pH was identical to the UV-vis spectrum of the Ru^{III} species generated from $\mathbf{4^{II}}$ during spectroelectrochemical experiments at pH 2.0 (Figure S26). ^{1}H NMR spectrum of $\mathbf{4^{III}}$ displayed broadened signals, typical for paramagnetic d^5 Ru^{III} species (Figure S18). Moreover, a paramagnetic EPR spectrum was observed for $\mathbf{4^{III}}$ (Figure 9), further confirming the oxidation state of the complex.

Surprisingly, at higher pH the Ru^{III} complex $\mathbf{4^{III}}$ is unstable and forms Ru^{II} species, as evident from the UV-vis spectra of the complex recorded over 4 h upon pH jump from pH 2.0 to 7.0 (Figure 5). Upon the pH jump an MLCT band with λ_{max} = 479 nm appeared over time along with changing ligand-based transition bands, resulting in a UV-vis spectrum closely resembling that of Ru^{II} complex $\mathbf{4^{II}}$ at pH 7.0, but with twice as low concentration (Figure 5, *left*). The kinetics of the transformation, as monitored by the change in the absorbance at 479 nm, displayed a complex multi-exponential character, precluding reliable fitting to a theoretical model (Figure S28). The changes in redox behavior of $\mathbf{4^{III}}$ upon the pH jump were subsequently monitored electrochemically (Figure S37), displaying formation of the Ru-aqua species (see Section 2.4), which was also observed for complex $\mathbf{4^{II}}$ upon repetitive CV cycling reaching potentials of electrocatalytic water oxidation (Section 2.3.1) or after CPE at 1.4 V (Section 2.4.2). The disappearance of the paramagnetic Ru^{III} species after the pH jump was also confirmed by EPR (Figure S30).

The above observations suggest a disproportionation type of reaction between the Ru^{III} species to form a Ru^{II} and a Ru^{IV} species, concomitant with formation of the Ru-aqua complex. The direct disproportionation of Ru^{III} species to Ru^{II} and Ru^{IV} is unlikely, given the large difference between the redox potentials of the $Ru^{III/II}$ and $Ru^{IV/III}$ couples with $\Delta E_{1/2} \approx 0.6$ V. Therefore, we propose that water slowly reacts with Ru^{III} complex $\mathbf{4^{III}}$ to form Ru^{III}–OH species (Eq. 2). In the Ru^{III} and Ru^{III}–OH mixture the latter is easier to oxidize, since $E_{pa}(Ru^{IV}{=}O/Ru^{III}{-}OH) = 0.95$ V (see Section 2.4.2) is significantly lower than $E_{1/2}(Ru^{IV/III}) = 1.32$ V, which results in formation of Ru^{IV}=O and Ru^{II} species (Eq. 3). The reverse transformation $Ru^{II} + Ru^{IV}{=}O \rightarrow Ru^{III} + Ru^{III}{-}OH$ is then thermodynamically possible, since $E_{pc}(Ru^{III/II}) \approx E_{pc}(Ru^{IV}{=}O/Ru^{III}{-}OH) \approx 0.7$ V, but the overall equilibrium is shifted to the products of the forward reaction due to the indicated difference in the E_{pa} values. The shifted equilibrium in the solution electron transfer reaction (Eq. 3) then provides the driving force for the otherwise unfavorable coordination of water to the Ru^{III} species (Eq. 2). Further, the sum of the UV-vis spectra of Ru^{II} complex $\mathbf{4^{II}}$ and Ru^{IV}=O complex $\mathbf{5^{IV}}$ generated spectroelectrochemically (see Section 2.4.1) resulted in a spectrum closely overlapping with the final UV-vis spectrum of $\mathbf{4^{III}}$ at 250 min after pH jump (Figure 3, *right*). In this experiment, however, absorbance of the $\mathbf{5^{IV}}$ species had to be normalized to twice as low concentration compared to species $\mathbf{4^{II}}$, indicating that stoichiometry of Eq. 2 and 3 is affected by some side-reaction, possibly slow oxidation of water by the Ru^{IV}=O species, as was observed previously for other WOCs.[3a,12] It is important to point out that even though the described transformations include formation of the Ru-aqua species already at the Ru^{III} state, the reaction is sufficiently slow on the CV timescale, consistent with the chemical reversibility of the $Ru^{III/II}$ couple of $\mathbf{4^{II}}$ at pH 7.0 observed during spectroelectrochemical measurements. The described transformations are extremely slow at low pH, which is reasonable, given that both of the reactions require abstraction of a proton.

$$Ru^{III} + H_2O \rightleftarrows Ru^{III}{-}OH + H^+ \quad (2)$$

$$Ru^{III} + Ru^{III}{-}OH \rightarrow Ru^{II} + Ru^{IV}{=}O + H^+ \quad (3)$$

2.4 Redox Properties and Catalytic Activity of the Ru-aqua Complex 5 Generated from Complex 4

2.4.1 Stoichiometric Generation of a Catalytically Active Ru-aqua Complex 5

Spectroelectrochemical measurements of Ru^{II} complex $\mathbf{4^{II}}$ between 0.52 and 1.06 V at pH 7.0 demonstrated full chemical

reversibility of the $Ru^{III/II}$ couple (Figure S44), similar to the measurements made at pH 2.0 (Figures S42 and S43), with a $Ru^{III/II}$ cathodic wave observed at ca. 0.70 V. When reaching potentials of up to 1.40 V (where the $Ru^{III} \rightarrow Ru^{IV}$ transition can occur) the reverse CV scan also displayed a cathodic wave at a similar potential; however, the change in the UV-vis absorption during the experiment at this potential range was dramatically different (Figure 6). Upon the CV scan from 1.00 to 1.40 V the UV-vis spectra displayed formation of Ru^{IV} species, but during the reverse scan from 1.40 to 1.00 V the Ru^{III} species were not replenished. Instead, the UV-vis spectum continued to change in the same manner as during the $Ru^{III} \rightarrow Ru^{IV}$ transition. We attribute this behavior to a water association reaction, which follows the $Ru^{III} \rightarrow Ru^{IV}$ transition (Eq. 4 and 5). The $Ru^{IV} \rightarrow Ru^{III}$ transition of the formed Ru-aqua species is then observed at significantly lower potential of ca. 0.7 V, consistent with better stabilization of the highly-oxidized metal center by the negatively charged hydroxo/oxo ligand (Eq. 6). A slight increase in the UV-vis absorbance at 479 nm, attributed to formation of non-aqua Ru^{II} species, was also observed by UV-vis on the reverse CV scan (Figure 6e). This is presumably because on the timescale of the spectroelectrochemical experiment not all of the formed Ru^{IV} species could be transformed into Ru^{IV}=O.

$$Ru^{III} - e^- \rightarrow Ru^{IV} \quad (4)$$

$$Ru^{IV} + H_2O \rightarrow Ru^{IV}{=}O + 2H^+ \quad (5)$$

$$Ru^{IV}{=}O + e^- + H^+ \rightarrow Ru^{III}{-}OH \quad (6)$$

For further catalytic studies, the Ru-aqua species **5** was generated stoichiometrically at pH 7.0 by CPE of complex $\mathbf{4}^{II}$ at 1.40 V (Figure S38). During electrolysis the non-aqua Ru^{II} complex $\mathbf{4}^{II}$ is transformed into Ru^{IV} and then Ru^{IV}=O species, which can catalyze water oxidation at the applied potential. Accordingly, the current increased over time due to accumulation of the active species and a decrease in pH of the solution was observed. The electrolysis was terminated when the current reached a plateau (pH of the final solution was then adjusted back to 7.0 prior to further experiments).

2.4.2 Evaluation of the Catalytically Active Ru-aqua Complex 5 Generated from Complex 4

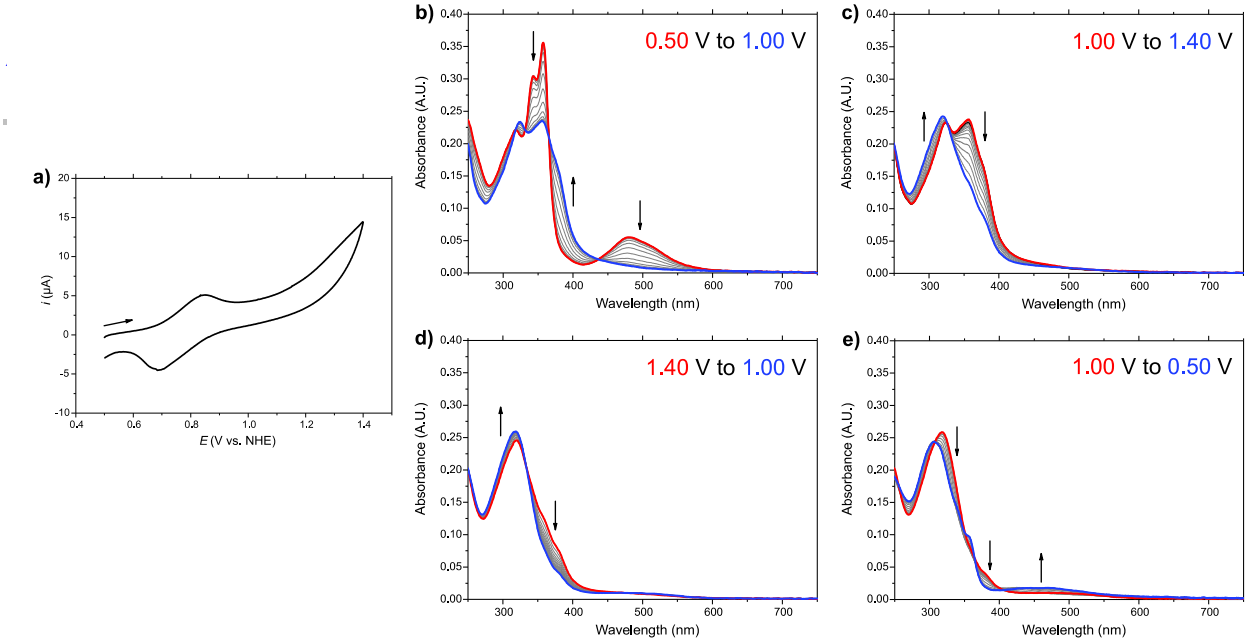

Figure 6. Spectroelectrochemical measurements of ca. 0.4 mM solution of complex $\mathbf{4}^{II}$ at pH 7.0 using OTTLE cell (see the Supporting Information for details). a) CV of complex $\mathbf{4}^{II}$ recorded at 0.002 V s^{-1} scan rate between 0.5 V and 1.4 V. b) Change in UV-vis absorbance during the anodic sweep from 0.5 to 1.0 V. c) Change in UV-vis absorbance during the anodic sweep from 1.0 to 1.4 V. d) Change in UV-vis absorbance during the cathodic sweep from 1.4 to 1.0 V. e) Change in UV-vis absorbance during the cathodic sweep from 1.0 to 0.5 V. Vertical arrows indicate the direction of change in UV-vis absorbance during CV scan.

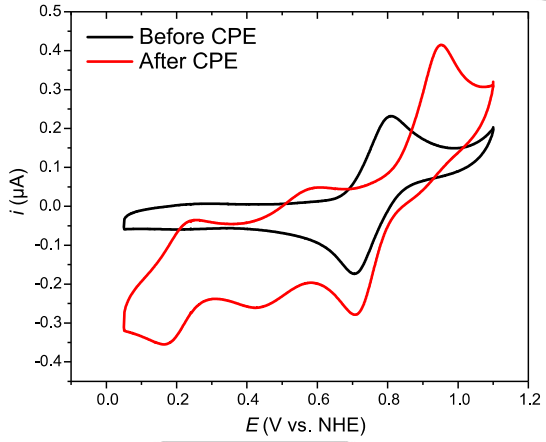

Figure 7. CV of 0.2 mM solution of complex $\mathbf{4}^{II}$ recorded at 0.05 V s^{-1} scan rate at pH 7.0 (before CPE) and CV of complex **5** (after CPE) generated from $\mathbf{4}^{II}$ by CPE at 1.40 V at pH 7.0.

A comparison of the CV of the solution of complex $\mathbf{4}^{II}$ before and after electrolysis revealed full transformation of the complex into the new Ru-aqua species **5** (Figure 7). A new irreversible couple appeared at the potentials close to the $Ru^{III/II}$ couple of complex **4**, with E_{pa} = 0.952 V and E_{pc} = 0.709 V. Based on spectroelectrochemical measurements this couple was assigned to the $Ru^{IV/III}$ transition, with λ_{max} = 307 nm for Ru^{III} and λ_{max} = 316 nm for Ru^{IV} species (Figure 8). Two other redox couples of smaller magnitude with $E_{1/2}$ = 0.202 and 0.518 V were assigned to two $Ru^{III/II}$ couples of different isomers of the Ru-aqua species. While the couple at 0.202 V is close to being quasi-reversible (ΔE_p = 0.071 V) the couple at 0.518 V represents an $E_rC_rE_rC_r$ square scheme (ΔE_p = 0.176 V, E_{pa} = 0.606 V, E_{pc} = 0.430 V). Spectroelectrochemical characterization of these couples was unfortunately prohibited by the narrow working potential window of the employed spectroelectrochemical cell. Importantly, the new species have the same potentials as those emerging upon repetitive cycling of complex $\mathbf{4}^{II}$ to the potentials of electrocatalytic water oxidation (Section 2.3.1) and upon pH jump from 2.0 to 7.0 for complex $\mathbf{4}^{III}$ (Section 2.3.2), confirming formation of the Ru-aqua species under these conditions.

The pH of the generated solution with Ru-aqua species was adjusted to variable values, and CV and DPV data was used to construct the Pourbaix diagram (Figure 12, *left*). The observed $Ru^{III/II}$ and $Ru^{IV/III}$ couples displayed a distinct pH-dependence close to −0.059 V per pH unit, although perturbed by coupled chemical reactions and close-lying pK_a values of the Ru^{II}, Ru^{III}, and Ru^{IV} complexes. As the carboxylate groups of the ligand are deprotonated at pH > 4, proton transfer was associated with the aqua ligand and the observed couples were assigned to

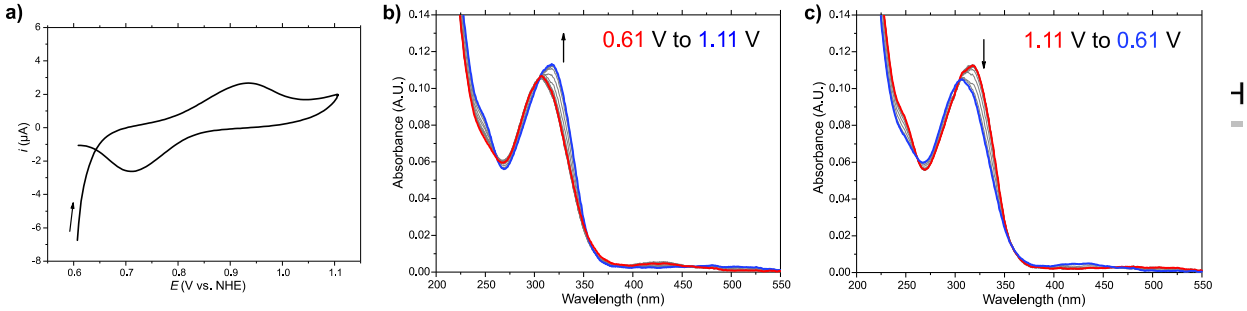

Figure 8. Spectroelectrochemical measurements of 0.2 mM solution of complex **5** generated from complex **4^{II}** by CPE at pH 7.0 using OTTLE cell (see the Supporting Information for details). a) CV of complex **5** recorded at 0.002 V s^{-1} scan rate between 0.61 V and 1.11 V. b) Change in UV-vis absorbance during the anodic sweep from 0.61 to 1.11 V. c) Change in UV-vis absorbance during the cathodic sweep from 1.11 to 0.61 V. Vertical arrows indicate the direction of change in UV-vis absorbance during CV scan.

Ru^{III}–OH/Ru^{II}–OH_2 and Ru^{IV}=O/Ru^{III}–OH transitions. The $Ru^{V/IV}$ couple displayed a pH-independence at pH 5–10, whereas at lower pH a slope of −0.059 V per pH unit was observed due to formation of a Ru^{IV}=OH species with pK_a = 5.1.

Complex **4^{II}** and the electrochemically generated complex **5** were also studied by ^{1}H NMR in an aqueous pD 7.0 phosphate buffer solution (Figures S14 and S20). In analogy to the ^{1}H NMR spectrum of **4^{II}** obtained in DMSO-d_6 upon addition of D_2SO_4, the ^{1}H NMR spectrum of **4^{II}** in aqueous solution was fully assigned, confirming the integrity of the complex in water. After generation of complex **5** by CPE the ^{1}H NMR spectrum displayed shifted and broadened signals due to the presence of the Ru^{III}–OH species, as observed by EPR. However, when the obtained species was reduced to the Ru^{II} state by excess ascorbic acid a diamagnetic spectrum identical to that of the initial ^{1}H NMR spectrum of Ru^{II} complex **4^{II}** was observed. This suggests that on the timescale of the experiment (ca. 3 min between addition of ascorbic acid and acquisition of the NMR spectrum) the Ru^{II}–OH_2 species are not stable and the water molecule dissociates from the metal center. Additional peaks were also observed in ^{1}H NMR spectra after generation of the Ru-aqua species and were still present upon reduction of the complex to the Ru^{II} state. However, these contaminants did not correspond to free pyridine (Figure S21), which is an expected product from decomposition of catalyst **5**.

Furthermore, the EPR spectrum of the Ru-aqua species **5** demonstrated a low intensity paramagnetic spectrum, suggesting the presence of Ru^{III}–OH species (Figure 9). Importantly, the EPR spectrum of these species was drastically different from the spectrum of the non-aqua Ru^{III} species at the same pH, suggesting that the generated Ru-aqua species is a mixture of Ru^{III}–OH and Ru^{IV}=O complexes.

2.4.3 Catalytic Activity of Complex 5

A CV of the electrochemically generated complex **5** up to 1.45 V demonstrated a largely increased catalytic current compared to the initial Ru^{II} complex **4^{II}** with an onset potential at ca. 1.25 V (Figure 10). Under repetitive cycling the redox waves of the Ru-aqua species were unchanged (except for a slight anodic shift due to the local change in pH during water oxidation), confirming that the catalytically active species was generated stiochiometrically during CPE and are stable on the experiment timescale.

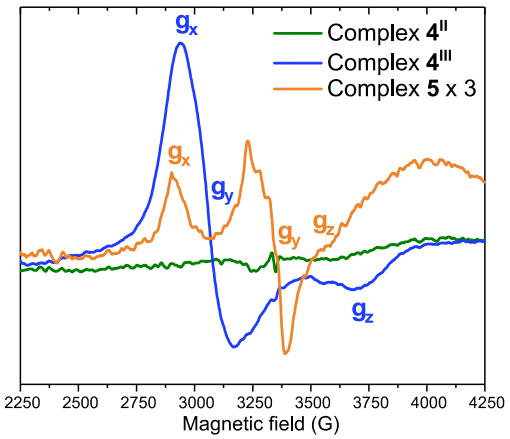

Figure 9. EPR spectra of complex **4^{II}** (green), **4^{III}** (blue), and **5** (orange) at pH 7.0.

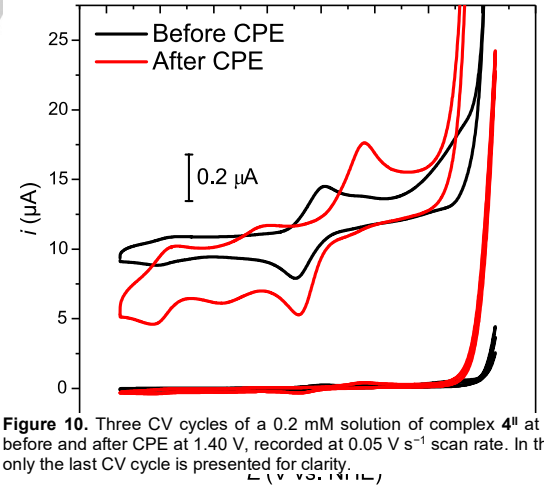

Figure 10. Three CV cycles of a 0.2 mM solution of complex **4^{II}** at pH 7.0 before and after CPE at 1.40 V, recorded at 0.05 V s^{-1} scan rate. In the inset only the last CV cycle is presented for clarity.

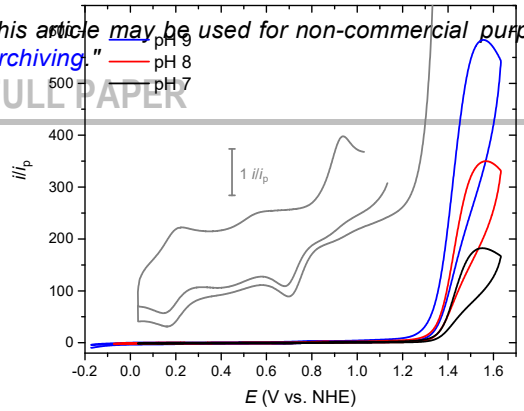

Figure 11. CV of 0.2 mM solutions of catalyst **5** recorded at 0.1 V s^{-1} at pH 7.0, 8.0 and 9.0.

The catalytic activity of complex **5** for water oxidation was evaluated using the foot-of-the-wave analysis (FOWA),[13] assuming O–O bond formation through WNA as the rate determining step (Figure 11 and Figures S45–S48, see the Supporting Information for details). As a result, concentration-independent TOF_{max} values of $1.4±0.4×10^3$, $9.3±0.3×10^3$, and $4.2±1.5×10^4$ s^{-1} were observed at pH 7, 8, and 9, respectively, while for the parent catalyst **2** TOF_{max} values of ca. $8×10^3$, $2.5×10^4$, and $5×10^4$ s^{-1} were found at pH 7, 8, and 10. The activities of the two catalysts are therefore similar given the sensitivity of the method and much greater than the activities of other WOCs operating via a WNA mechanism, as evident from the catalytic Tafel plot (Figure S49). Furthermore, the catalytic activity of complex **5** was evaluated on a longer timescale by CPE at 1.45 V with monitoring of the evolved oxygen by a gas-phase Clark electrode (Figure S50). After 30 min of electrolysis 98% faradaic efficiency was observed with TON = 9.3, based on the total amount of the catalyst in the anode compartment. An intrinsic TON of the catalyst under the employed bulk electrolysis conditions was calculated by estimating the amount of catalyst that participates in the catalysis at the electrode surface (Eq. S7) and exceeded 4 million. The CV of the catalyst solution before and after CPE remained unchanged, highlighting stability of complex **5** under the studied catalytic conditions (Figure S51).

3 Discussion

Given the similarity of the catalytic activity of catalysts **2** and **5**, it is noteworthy to compare the redox properties of the complexes in activated (**2** and **5**) and non-activated forms (**1** and **4**). As evident from the Pourbaix diagrams of the complexes (Figure 12), both $Ru^{III/II}$ and $Ru^{IV/III}$ couples for complex **4** are ca. 0.2 V more positive than the corresponding couples for catalyst **1**. This is in line with the expected weakening of the Ru–O bonds in complex **4** due to a change from stable five-membered rings in catalyst **1** to highly strained six-membered rings in catalyst **4**. This is also supported by the X-ray crystal structures of the complexes at the Ru^{III} state, where the tda^{2-} ligand in catalyst **1** adopts a κ-N^3O^2 coordination mode and the $Hmcbp^-$ ligand in catalyst $\mathbf{4}^{III}$ coordinates to the ruthenium center in a κ-N^3O mode, providing an open site for coordination of water to the metal center and formation of Ru-aqua species **5**. The difference in the potentials of $Ru^{III/II}$ and $Ru^{IV/III}$ couples for the complexes could also be ascribed to the difference in the electronic properties between the 2,2′:6′,2″-terpyridine (tpy) ligand core in catalyst **1** and Mebimpy ligand core in catalyst **4**. However, for the related complexes $[Ru(tpy)(py)_3]^{2+}$ and $[Ru(Mebimpy)(pic)_3]^{2+}$ an opposite trend in the redox potentials for the $Ru^{III/II}$ couple was observed, with $E_{1/2}(Ru^{III/II})$ of $[Ru(tpy)(py)_3]^{2+}$ being ca. 0.25 V more positive than $E_{1/2}(Ru^{III/II})$ of $[Ru(Mebimpy)(pic)_3]^{2+}$. The latter supports that the elevated potentials for complex **4** are indeed due to less efficient stabilization of the metal center at high oxidation states by the more loosely bound carboxylate ligands.

The elevated potential for the $Ru^{III/II}$ couple for complex **4**

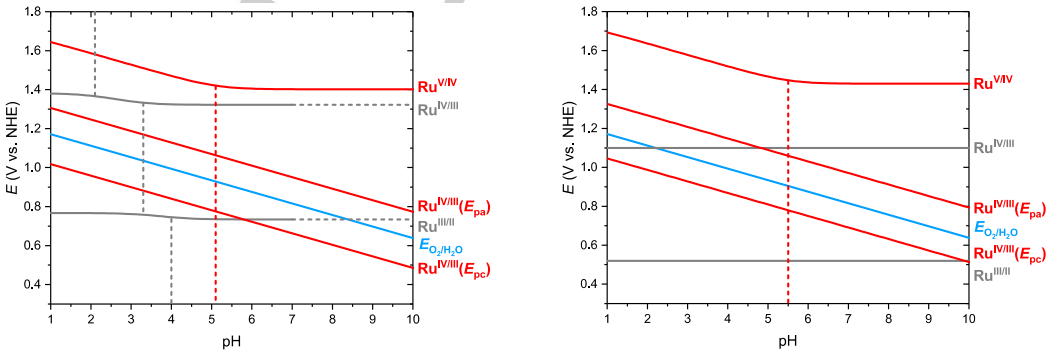

Figure 12. Pourbaix diagrams for complexes **5** (left) and **2** (right, simulated and extrapolated for pH < 3 using experimental data for pH 3–11 from Ref. [3a]). Grey lines represent redox potentials of the non-aqua ruthenium species and red lines represent redox potentials of the aqua ruthenium species. The thermodynamic potential of water oxidation is shown with the blue line.

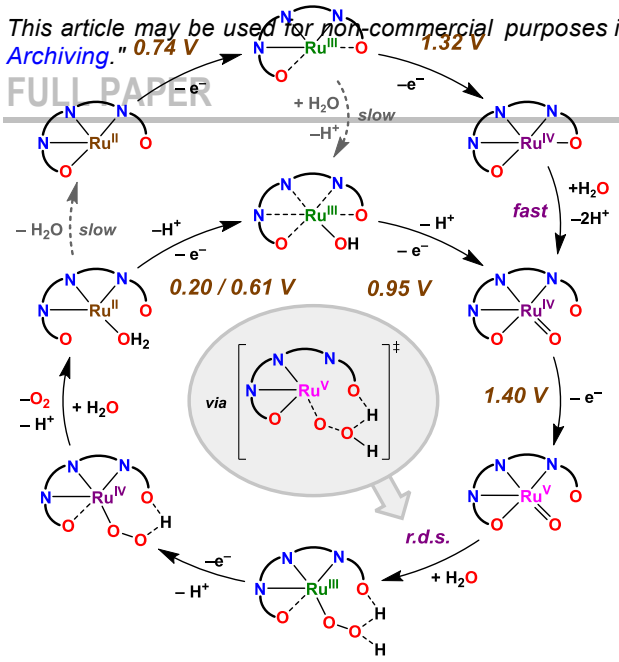

Scheme 1. Summary of the proposed transformations of the complexes derived from **4**, including catalyst activation and the catalytic cycle of water oxidation. The $mcbp^{2-}$ ligand is represented with arcs and the axial pyridine ligands are omitted for clarity. Dashed lines indicate simultaneously formed and broken bonds.

together with the weakened Ru–O bonds at the Ru^{III} oxidation state allows formation of Ru-aqua species **5** already at the Ru^{III} oxidation state of **4**, which has not been observed for catalyst **1**. The reaction is slow on a typical timescale of electrochemical measurements but could be observed on longer timescale by UV-vis for Ru^{III} complex $\mathbf{4^{III}}$. Due to the close-lying potentials of the $Ru^{IV/III}$ couple of Ru-aqua species **5** and the $Ru^{III/II}$ couple of catalyst **4** the energetically unfavorable reaction $Ru^{III} + H_2O \rightarrow Ru^{III}–OH + H^+$ is driven to completion by the following disproportionation reaction $Ru^{III} + Ru^{III}–OH \rightarrow Ru^{II} + Ru^{IV}=O + H^+$, as described in Section 2.3.2. Furthermore, a large difference in rates for the formation of the catalytically active complexes **2** and **5** was also observed at the Ru^{IV} state of the catalyst precursors. Complex **4** could be fully activated within ca. 4 min during the spectroelectrochemical measurements reaching the Ru^{IV} state, while for complex **1** a 10 h electrolysis was required to transform only ⅓ of the initial complex into the active species **2** at pH 7. Importantly, the slow activation of complex **1** limited performance of hybrid anodes based on **1** due to decrease of catalyst loading in course of its activation.

For the activated catalysts **2** and **5** a striking similarity of the pH-dependent redox potentials was observed, as evident from their Pourbaix diagrams (Figure 12). Herein, it is important to mention that due to incomplete activation of catalyst **1** a reliable assignment of the newly formed redox transitions was extremely challenging: an anodic wave at ca. 0.9 V and a cathodic wave at ca. 0.7 V formed during catalyst activation at pH 7 appeared in close proximity to the still present $Ru^{III/II}$ and $Ru^{IV/III}$ couples of **1** and were assigned to the $Ru^{IV/III}$ and $Ru^{III/II}$ transitions, respectively. However, we believe that given the nearly identical pH-dependent electrochemical response from catalyst **5**, these anodic and cathodic waves represent an electrochemically irreversible $Ru^{IV/III}$ couple, unambiguously identified for catalyst **5** by spectroelectrochemical measurements. Presumably, the $Ru^{III/II}$ couple for the activated catalyst **2** is then nearly entirely buried under the $Ru^{III/II}$ couple of the non-activated complex **1**.

Given these observations, we propose that the catalytic cycle for catalyst **5** should resemble the catalytic cycle established for catalyst **2** with the help of DFT calculations (Scheme 1). The electrochemically generated $Ru^{IV}=O$ complex **5** undergoes one-electron oxidation to a $Ru^{V}=O$ species, which is responsible for the rate-limiting O–O bond formation step via WNA. Importantly, the latter is facilitated by the simultaneous transfer of a proton from water to one of the carboxylate groups by an *i*-APT mechanism, significantly lowering the activation energy of the reaction. The formed $Ru^{III}–OOH_2$ hydroperoxide species undergoes fast one-electron/one-proton oxidation to $Ru^{IV}–OOH$, while both of the hydroperoxide species are stabilized by the hydrogen bonding to the dangling carboxylate ligand. Oxygen release from the $Ru^{IV}–OOH$ and coordination of a new water molecule to ruthenium results in formation of $Ru^{II}–OH_2$ species. These species then undergo two one-electron/one-proton oxidation steps, reforming the $Ru^{IV}=O$ complex and completing the catalytic cycle.

4 Conclusions

A new highly active water oxidation catalyst **5** was generated from the precursor complex **4**. The high activity and stability of the catalyst was demonstrated and the redox behavior of the Ru-non-aqua and aqua species was studied in detail. The newly developed catalyst represents a significant improvement to the state-of-the-art catalyst **1**, which could not be activated fully, prohibiting detailed mechanistic studies. On the other hand, activation of catalyst **4** proceeds fully at mild conditions, resulting in the active catalyst **5**, reaching $TOF_{max} \approx 40\ 000\ s^{-1}$ at pH 9. Moreover, the developed benzimidazole-based $mcbp^{2-}$ ligand provides a versatile and synthetically accessible framework for the structure alterations by, for example, replacement of the N-Me groups. Modification of these groups can then be used for tuning steric and electronic properties of the ligand as well as anchoring of the catalyst onto electrode surfaces.

Acknowledgements

B.Å. thanks Swedish Research Council (621-2013-4872), Stiftelsen Olle Engkvist Byggmästare, and the Knut and Alice Wallenberg Foundation (2011.0038) for the financial support.

A.L. thanks MINECO, FEDER and AGAUR for grants CTQ2016-80058-R, CTQ2015-73028-EXP, SEV 2013-0319, ENE2016-82025-REDT, CTQ2016-81923-REDC, and 2017-SGR-1631. A.S. thanks Stiftelsen Längmanska Kulturfonden (BA17-1321) for a PhD exchange scholarship. A.A.B. thanks Swedish Institute (Visby Programme, 03572/2016) for a postdoctoral travel grant and the Russian Foundation for Basic Research (18-03-01076).

Keywords: artificial photosynthesis • water oxidation • ruthenium • molecular catalysis

[1] a) N. S. Lewis, *Science* **2016**, *351*, 353–360; b) J. R. McKone, D. C. Crans, C. Martin, J. Turner, A. R. Duggal, H. B. Gray, *Inorg. Chem.* **2016**, *55*, 9131–9143; c) O. Ellabban, H. Abu-Rub, F. Blaabjerg, *Renewable and Sustainable Energy Reviews* **2014**, *39*, 748–764; d) N. L. Panwar, S. C. Kaushik, S. Kothari, *Renewable and Sustainable Energy Reviews* **2011**, *15*, 1513–1524; e) N. S. Lewis, D. G. Nocera, *Proc. Natl. Acad. Sci. U.S.A.* **2006**, *103*, 15729–15735.

[2] a) P. Garrido-Barros, C. Gimbert-Suriñach, R. Matheu, X. Sala, A. Llobet, *Chem. Soc. Rev.* **2017**, *46*, 6088–6098; b) I. Funes-Ardoiz, P. Garrido-Barros, A. Llobet, F. Maseras, *ACS Catal.* **2017**, *7*, 1712–1719; c) L. Tong, R. P. Thummel, *Chem. Sci.* **2016**, *7*, 6591–6603; d) M. D. Kärkäs, B. Åkermark, *Dalton Trans.* **2016**, *45*, 14421–14461; e) M. Yamamoto, K. Tanaka, *ChemPlusChem* **2016**, *81*, 1028–1044; f) X. Wu, F. Li, B. Zhang, L. Sun, J. *Photochem. Photobiol. C: Photochem. Rev.* **2015**, *25*, 71–89; g) J. D. Blakemore, R. H. Crabtree, G. W. Brudvig, *Chem. Rev.* **2015**, *115*, 12974–13005; h) D. L. Ashford, M. K. Gish, A. K. Vannucci, M. K. Brennaman, J. L. Templeton, J. M. Papanikolas, T. J. Meyer, *Chem. Rev.* **2015**, *115*, 13006−13049; i) M. D. Kärkäs, O. Verho, E. V. Johnston, B. Åkermark, *Chem. Rev.* **2014**, *114*, 11863–12001.

[3] a) R. Matheu, M. Z. Ertem, J. Benet-Buchholz, E. Coronado, V. S. Batista, X. Sala, A. Llobet, *J. Am. Chem. Soc.* **2015**, *137*, 10786–10795; b) J. Creus, R. Matheu, I. Peñafiel, D. Moonshiram, P. Blondeau, J. Benet-Buchholz, J. García-Antón, X. Sala, C. Godard, A. Llobet, *Angew. Chem. Int. Ed.* **2016**, *55*, 15382–15386; c) L. Francàs, R. Matheu, E. Pastor, A. Reynal, S. Berardi, X. Sala, A. Llobet, J. R. Durrant, *ACS Catal.* **2017**, *7*, 5142–5150; d) R. Matheu, I. A. Moreno-Hernandez, X. Sala, H. B. Gray, B. S. Brunschwig, A. Llobet, N. S. Lewis, *J. Am. Chem. Soc.* **2017**, *139*, 11345–11348; e) R. Matheu, M. Z. Ertem, C. Gimbert-Suriñach, J. Benet-Buchholz, X. Sala, A. Llobet, *ACS Catal.* **2017**, *7*, 6525–6532; f) S. Grau, S. Berardi, A. Moya, R. Matheu, V. Cristino, J. José Vilatela, C. A. Bignozzi, S. Caramori, C. Gimbert-Suriñach, A. Llobet, *Sustainable Energy Fuels*, **2018**, *2*, 1979–1985.

[4] a) Z. Chen, J. J. Concepcion, J. W. Jurss, T. J. Meyer, *J. Am. Chem. Soc.* **2009**, *131*, 15580–15581; b) J. J. Concepcion, J. W. Jurss, M. R. Norris, Z. Chen, J. L. Templeton, T. J. Meyer, *Inorg. Chem.* **2010**, *49*, 1277–1279; c) D. M. Ryan, M. K. Coggins, J. J. Concepcion, D. L. Ashford, Z. Fang, L. Alibabaei, D. Ma, T. J. Meyer, M. L. Waters, *Inorg. Chem.* **2014**, *53*, 8120–8128; d) D. L. Ashford, A. M. Lapides, A. K. Vannucci, K. Hanson, D. A. Torelli, D. P. Harrison, J. L. Templeton, T. J. Meyer, *J. Am. Chem. Soc.* **2014**, *136*, 6578–6581; e) S. E. Bettis, K. Hanson, L. Wang, M. K. Gish, J. J. Concepcion, Z. Fang, T. J. Meyer, J. M. Papanikolas, *J. Phys. Chem. A* **2014**, *118*, 10301–10308; f) S. E. Bettis, D. M. Ryan, M. K. Gish, L. Alibabaei, T. J. Meyer, M. L. Waters, J. M. Papanikolas, *J. Phys. Chem. C* **2014**, *118*, 6029−6037; g) A. M. Lapides, B. D. Sherman, M. K. Brennaman, C. J. Dares, K. R. Skinner, J. L. Templeton, T. J. Meyer, *Chem. Sci.* **2015**, *6*, 6398–6406; h) M. S. Eberhart, K.-R. Wee, S. Marquard, K. Skinner, D. Wang, A. Nayak, T. J. Meyer, *ChemSusChem* **2017**, *10*, 2380–2384; i) Z. Chen, J. J. Concepcion, H. Luo, J. F. Hull, A. Paul, T. J. Meyer, *J. Am. Chem. Soc.* **2010**, *132*, 17670–17673; j) J. J. Concepcion, M.-K. Tsai, J. T. Muckerman, T. J. Meyer, *J. Am. Chem. Soc.* **2010**, *132*, 1545–1557; k) W. Song, A. Ito, R. A. Binstead, K. Hanson, H. Luo, M. K. Brennaman, J. J. Concepcion, T. J. Meyer, *J. Am. Chem. Soc.* **2013**, *135*, 11587−11594; l) J. J. Concepcion, R. A. Binstead, L. Alibabaei, T. J. Meyer, *Inorg. Chem.* **2013**, *52*, 10744−10746; m) Z. Chen, J. J. Concepcion, N. Song, T. J. Meyer, *Chem. Commun.* **2014**, *50*, 8053–8056; n) K. L. Materna, B. J. Brennan, G. W. Brudvig, *Dalton Trans.* **2015**, *44*, 20312–20315.

[5] L. Duan, Y. Xu, L. Tong, L. Sun, *ChemSusChem* **2011**, *4*, 238–244.

[6] L. Francàs, R. M. González-Gil, D. Moyano, J. Benet-Buchholz, J. García-Antón, L. Escriche, A. Llobet, X. Sala, *Inorg. Chem.* **2014**, *53*, 10394–10402.

[7] In theory for *n*-electron diffusional couples $\Delta E_p = 0.059/n$ V and $W_{1/2} = 0.094/n$ V (limiting value for DPV pulse amplitude $\Delta E \rightarrow 0$).

[8] a) N. Planas, L. Vigara, C. Cady, P. Miró, P. Huang, L. Hammarström, S. Styring, N. Leidel, H. Dau, M. Haumann, L. Gagliardi, C. J. Cramer, A. Llobet, *Inorg. Chem.* **2011**, *50*, 11134–11142; b) K. J. Takeuchi, M. S. Thompson, D. W. Pipes, T. J. Meyer, *Inorg. Chem.* **1984**, *23*, 1845–1851.

[9] It is important to mention that during spectroelectrochemical studies the slow scan rate (2 mV s^{-1}) and the geometry of the cell (ca. 0.2 mm optical path through the cell containing Pt mesh working electrode) ensures bulk electrolysis of all the electroactive material at any given potential. However, due to the cell geometry and sensitivity of the Ag wire pseudo-reference electrode the peak separation is not always consistent with the CV measurements made with planar working electrodes under diffusional control (see the Supporting Information for details).

[10] D. R. Weinberg, C. J. Gagliardi, J. F. Hull, C. F. Murphy, C. A. Kent, B. C. Westlake, A. Paul, D. H. Ess, D. G. McCafferty, T. J. Meyer, *Chem. Rev.* **2012**, *112*, 4016–4093.

[11] a) D. H. Evans, *Chem. Rev.* **1990**, *90*, 739–751; b) A. J. Bard, L. R. Faulkner. Electrode Reactions with Coupled Homogeneous Chemical Reactions. In *Electrochemical Methods: Fundamentals and Applications* (2nd ed.); John Wiley & Sons: New York, 2001; pp 471–533.

[12] a) S. Roeser, P. Farras, F. Bozoglian, M. Martínez-Belmonte, J. Benet-Buchholz, A. Llobet, *ChemSusChem* **2011**, *4*, 197−207; b) P. Farras, S. Maji, J. Benet-Buchholz, A. Llobet, *Chem. – Eur. J.* **2013**, *19*, 7162−7172.

[13] a) C. Costentin, S. Drouet, M. Robert, J.-M. Saveant, *J. Am. Chem. Soc.* **2012**, *134*, 11235−11242; b) R. Matheu, S. Neudeck, F. Meyer, X. Sala, A. Llobet, *ChemSusChem* **2016**, *9*, 3361–3369.

FULL PAPER

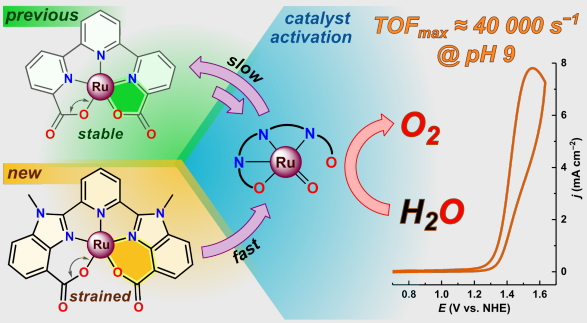

A. Shatskiy, A. A. Bardin, M. Oschmann, R. Matheu, J. Benet-Buchholz, L. Eriksson, M. D. Kärkäs, E. V. Johnston, C. Gimbert-Suriñach, A. Llobet, B. Åkermark**

Page No. – Page No.

Electrochemically-Driven Water Oxidation by a Highly Active Ruthenium-Based Catalyst